The electric field strength in orifice-like nanopores of ultrathin membranes

2015 Nanotechnology 26 045704

(http://iopscience.iop.org/0957-4484/26/4/045704)

IOP Publishing Nanotechnology
Nanotechnology **26** (2015) 045704 (9pp) doi:10.1088/0957-4484/26/4/045704

The electric field strength in orifice-like nanopores of ultrathin membranes

Jirachai Getpreecharsawas[1], James L McGrath[2] and David A Borkholder[1,2]

[1] Microsystems Engineering, Rochester Institute of Technology, Rochester, New York 14623, USA
[2] Department of Biomedical Engineering, University of Rochester, Rochester, New York 14627, USA

E-mail: david.borkholder@rit.edu

Received 25 August 2014, revised 20 November 2014
Accepted for publication 24 November 2014
Published 5 January 2015

Abstract

Here we show that the electric field inside an ultrathin membrane is weaker than conventional theory would predict, and that the reduced field is predictive of measured electroosmotic flow rates. Our theoretical analysis shows that the electric field inside a charged nanopore is affected by end effects and dependent on the Dukhin number Du when the pore length-to-diameter aspect ratio λ is less than 80 for $Du \ll 1$ or 300 for $Du \gg 1$. The electric field follows an unconventional scaling law; it no longer scales uniformly with the thickness of membrane, but with the local value of λ for each nanopore.

Keywords: electroosmosis, orifice-like nanopore, short-pore effect, ultrathin membrane

(Some figures may appear in colour only in the online journal)

1. Introduction

The magnitude of the electric field within porous, charged media determines the flow rate of an electroosmotic pump (EOP). Requiring no moving parts and causing no dispersion, EOPs are often preferable to pressure-driven transport for miniaturization efforts such as point-of-care diagnostics. The growing demand for on-chip EOPs, however, faces an arduous challenge due to its high voltage requirements (typically ~1 kV) [1]. Lowering the operating voltage necessitates a more efficient design of the entire EOP including the transport mechanism itself. Previous work has focused on redesigning the electroosmosis-inducing media [2], using different electrolytes [3], and reducing the spacing between electrodes [4, 5]. We have recently shown that the use of a molecularly thin (~15 nm) silicon membrane in an EOP produces the required field strengths at dramatically lower voltages (~10 V) [6]. EOPs produced with these highly permeable membranes are expected to be useful for on-chip pumping applications that do not have significant backpressure requirements.

The electric field in lossy media like electrolyte solutions depends on both the current density and the gradient of the electric potential. Thus simply decreasing the membrane thickness to achieve higher field strength will not be straightforward if the local current density is also affected. The conventional long pore (CLP) theory assumes that the pore has very high pore length-to-diameter aspect ratio in order to simplify its derivation [7]. This assumption underestimates the end effects inherited to the short nanopore. A more generalized model is proposed by compensating for the hydrodynamic end effects (HEE), which incur the extra pressure load at either end of the pore [8–10]. Even though the HEE model is valid for the nanopore with a lower aspect ratio than the CLP model is, it is still not valid for the orifice-like nanopore with its aspect ratio less than 1. The electric field inside a short nanopore can be reduced by an access resistance [11, 12], which is negligible compared to the pore resistance for a long pore, but not for a short pore [13]. A recent theoretical study also showed that the surface current density at a discontinuous charged surface, like at the entrance and exit of a charged nanopore, was greatly reduced decreasing the tangential electric field near the discontinuity [14]. It requires the transverse electric field to drive more ions from/to the bulk to maintain the conservation of charge within the nanopore. The tangential electric field regains the strength of the applied field eventually deep inside the long pore [14, 15]. However, for short nanopores this tangential field remains weakened. In this work we analytically combine the effects of the access resistance—discontinuity-induced tangential field weakening—and HEE with numerical simulation and experimental verification of the comprehensive model.

2. Methods

2.1. Experiment protocol

The electric field in a single orifice-like nanopore has not been well examined experimentally and its behavior in a thin porous membrane containing a multiple nanopores is unexplored. Our work focuses on investigating the electric field behavior near short pores for the purpose of understanding the ability of nanoporous ultrathin membranes to support electroosmosis (EO) [6]. In the experimental investigation, the electric field strength is deduced from the EO flow rates induced by a 15 nm thick porous nanocrystalline silicon (pnc-Si) membrane [16] with a mean pore length-to-diameter aspect ratio of 0.7 under various potentiostatic conditions (see appendix (A) for the detailed experiment protocol). The measured flow rates are then compared with those predicted by the CLP transport theory and more advanced models that include end effects for short pores. In addition to the access resistance which affects the electric field in pores, our models include the HEE [8–10] to account for an extra pressure drop at the entrance and exit of the short pores. We find that the inclusion of both electrical and hydrodynamic short-pore effects (SPE) is essential to predicting EO rates through ultrathin membranes.

2.2. Numerical simulation

The electric field inside the orifice-like nanopores of the ultrathin membrane is suspected to be less than the conventional calculation. The finite element simulations clarify this suspicion and elucidate the physics underlying the attenuated field strength. This numerical study uses electrokinetic theory to examine the concentration of ions and how the electric field near the membrane and within the nanopore is affected by the conductivity of the solution inside the nanopore. The concentration profiles of ions are prescribed by the charged surface of pore wall and membrane, and can be determined by solving Poisson–Nernst–Planck (PNP) equations. Over the charged surface, cations and anions distribute differently under the influence of diffusion from the gradient of their concentration $c_{\pm}$, migration under the gradient of the intrinsic potential ψ, and convection due to the velocity profile $\mathbf{v}$ of solvent according to the Nernst–Planck (NP) equation, $\mathbf{j}_{\pm} = -D_{\pm}\nabla c_{\pm} - z_{\pm}\left(D_{\pm}/RT\right)Fc_{\pm}\nabla\psi + \mathbf{v}c_{\pm}$, describing their ionic flux $\mathbf{j}_{\pm}$ where $D_{\pm}$ and $z_{\pm}$ denote their diffusion coefficients and valence numbers, and R, T, and F stand for the universal gas constant, absolute temperature, and Faraday's constant, respectively. Influenced by the electrostatics, the permittivity ε of solvent and the volume charge density, $\rho = F(z_+c_+ + z_-c_-)$, of ions in the electrolyte solution dictates the intrinsic potential ψ as described by the Poisson equation, $\nabla\cdot(\varepsilon\nabla\psi) = -\rho$. Unlike the intrinsic potential, the applied potential ϕ produces the electric field, $\mathbf{E} = -\nabla\phi$, corresponding to the current density, $\mathbf{J} = \sigma\mathbf{E}$, with the conductivity, $\sigma = \Lambda_+c_+ + \Lambda_-c_-$, of the profiles obtained from solving PNP equations, where $\Lambda_{\pm}$ represent the molar conductivities. It is worth noting that the convective flux of ions due to the creeping flow is negligible and is omitted from the simulations to reduce the computational time and complexity.

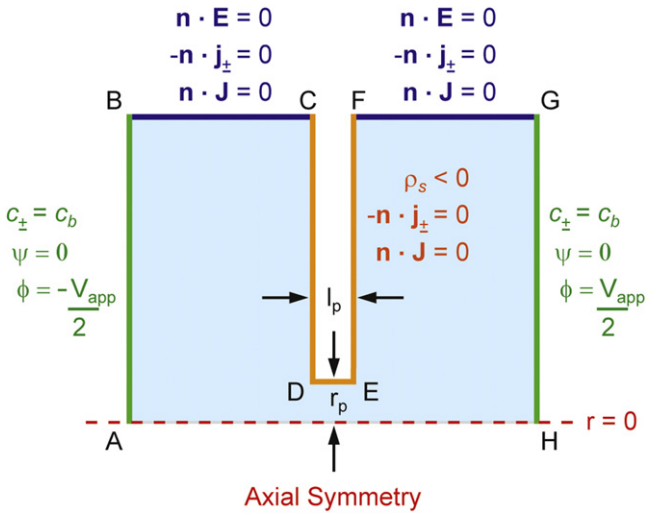

Figure 1. The schematic shows the axisymmetric domain and boundary conditions used in the numerical study of the electric field **E** inside a single orifice-like nanopore with the pore length l_p and radius r_p. The voltage of V_{app} is applied across the boundaries AB and GH. The membrane and its single nanopore are defined by the boundaries CD, DE, and EF with the negative surface charge density of ρ_s. The boundaries BC and FG contain no surface charge. The intrinsic potential ψ caused by the charged surface is defined with respect to that on the boundaries AB and GH, assumed to have a constant bulk concentration c_b. All the boundaries except AB, GH, and AH are assumed to have no ionic flux $\mathbf{j}_{\pm}$ and no current density **J**. The symbol **n** denotes a unit vector normal to a given boundary and pointing into the domain.

Figure 1 illustrates the domain, which is axisymmetric along the boundary AH, used in the simulations and all the respective boundary conditions. The electrolyte is aqueous NaCl with the bulk concentration of c_b, which is held constant at boundaries AB and GH to which the intrinsic potential ψ is referred. Also along the boundaries AB and GH, the potentials of $-V_{app}/2$ and $V_{app}/2$ are applied. The membrane is defined by the boundaries CD and EF with its nanopore wall along the boundary DE; all contain the negative surface charge density of ρ_s with no flux and no current flowing through. The boundaries BC and FG representing the extending reservoir are assumed to have no flux, no current, and no electric field in the direction perpendicular to these boundaries.

3. Results and discussion

3.1. SPE on EO flow rates

It was found that the measured flow rates of EO induced by the 15 nm thick pnc-Si membrane using 1 mM NaCl aqueous solution with neutral pH were uncharacteristically lower than the conventionally predicted by CLP and HEE transport models as shown in figure 2.

The conventional calculation of the electric field across the membrane is found by dividing the Ohmic potential drop

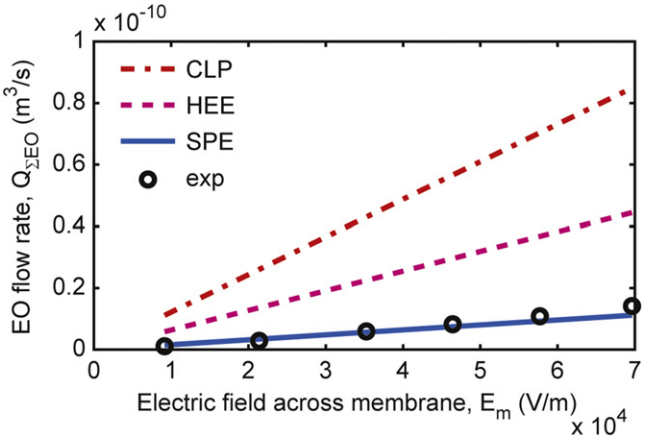

Figure 2. Accounting for short-pore effects results in good agreement between theoretical predictions of EO flow rates and experiments. Each measured flow rate is plotted with respect to the electric field across the membrane, which is estimated from the Ohmic potential drop divided by the membrane thickness. The symbols CLP, HEE, and SPE represent the predicted results from the conventional long pore theory, additionally with hydrodynamic end effects compensated, and with short-pore effects compensated (this work), respectively.

[17] across the membrane by the membrane thickness [18]. The potential drop across the membrane in turn was found by multiplying the current measured between electrodes with total membrane resistance which includes the access resistance of nanopores. The total resistance of each nanopore is predicted from the bulk solution conductivity and surface conductivity of charged walls of membrane nanopores according to the well-established theory [13]. Taking the pore-size distribution of the membrane into account yields the total resistance of the membrane [6].

3.2. Numerical simulations of concentration profiles and electric field within a single nanopore

The simulations reveal that the electric field inside the pore is impacted by both Dukhin number, $Du = (\sigma_s/\sigma_b)/r_p$– the ratio of the surface conductivity σ_s to the bulk conductivity σ_b divided by the pore radius [19]—and pore aspect ratio, $\lambda = l_p/2r_p$, (figure 3). This phenomenon occurs because the electric field is sensitive to the conductivity of medium; the ability of ions to diffuse from the bulk to the interior of short pores impacts the conductivity of the pore interior. This effect is more pronounced at higher bulk ion concentrations as seen in the first and second rows of figure 3, than it is at low bulk concentrations (the third row of figure 3).

Dukhin number indicates the ratio of the electric double layer (EDL) thickness to the pore radius [13]. When Du is much smaller than unity, usually at high bulk concentrations (the first row of figure 3), the majority of the nanopore is filled with the bulk solution and the electrolyte is nearly uniform across the orifice-like and both long nanopores. At moderate Du (the second row of figure 3), the EDL extends more prominently into the mid-pore region than in the regions near the nanopore entrance and exit, which are in direct contact with the bulk. The conductivity of the mid-pore region is therefore diverse from that of pore-end regions. At high Du (the third row of figure 3), the EDL becomes overlapped and screens the electrolyte inside the charged orifice-like and long nanopores from the bulk; the conductivity in the regions near the nanopore entrance and exit is influenced by that in the mid-pore region instead. Therefore, the conductivity across the membrane varies slightly from that in the mid-pore region.

Regardless of the Dukhin number, the axial component of the electric field is significantly weaker along the centreline of an orifice-like nanopore than near the pore walls. In contrast, the axial component of the electric field is nearly uniform across the pore cross-section for long pores (figure 3). The first column of figure 3 illustrates how converging and diverging field lines at the pore entrance and exit affect the field lines in the mid-pore region to give diminished field strength at the pore centreline. Therefore, the average electric field over the cross-sectional area of a short pore will be significantly lower than the conventional estimate assuming a uniform field.

3.3. SPE analytical model for field strength within a nanopore

In addition to our computational model, we have developed and solved an analytical model describing the impact of pore geometry on field strength. We begin by neglecting SPE, as in the CLP [7] and charge regulation [20–24] theories. With this assumption, the transport of solvent and ions in a single charged nanopore can be derived by the one-dimensional Navier–Stokes (NS) and NP equations, respectively. Fluid and ion transport are described in terms of the volumetric flow rate Q_i of the solvent, ionic flux N_i, and ionic current I_i as a function of the gradients of hydrostatic pressure P_i and osmotic pressure π_i in addition to electric potential ϕ_i being applied externally. Only the axial components of NS equations are needed to prescribe the velocity profile v_i of solvent, which is driven by Coulomb forces on the ions in the diffuse layer. The transport equation for the flow rate is then found with $Q_i = 2\pi \int_0^{r_i} v_i r \mathrm{d}r$. It is important to note that the hydrostatic pressure term in the NS equations is modeled as a sum of the partial pressure of solvent and the osmotic pressure of ions [7]. Similarly, the NP equations for the flux density of cation j_+ and anion j_- in the binary symmetric electrolyte solution, with valence number $z_+ = -z_- = z$, give rise to transport equations for the ionic flux $N_i = 2\pi \int_0^{r_i} \left(j_+ + j_-\right) r \mathrm{d}r$ and the ionic current $I_i = 2\pi z F \int_0^{r_i} \left(j_+ - j_-\right) r \mathrm{d}r$. All three CLP transport equations are expressed in matrix form as

$$\begin{bmatrix} Q_i \\ N_i \\ I_i \end{bmatrix} = \frac{1}{l_p} \begin{bmatrix} K_{11} & K_{12} & K_{13} \\ K_{21} & K_{22} & K_{23} \\ K_{31} & K_{32} & K_{33} \end{bmatrix} \begin{bmatrix} \Delta P_i \\ \Delta \pi_i \\ \Delta \phi_i \end{bmatrix}, \tag{1}$$

where the K coefficients are defined in appendix (B). Notably, the coefficient K_{33} characterizes the conductivity of a long, charged nanopore emphasizing the contribution from the convection $K_{33,\mathrm{conv}}$, (B.10), in addition to those from the concentration profiles, $\pi r_i^2 \left(\Lambda_+ \bar{c}_+ + \Lambda_- \bar{c}_-\right)$, where $\Lambda_\pm$ denotes

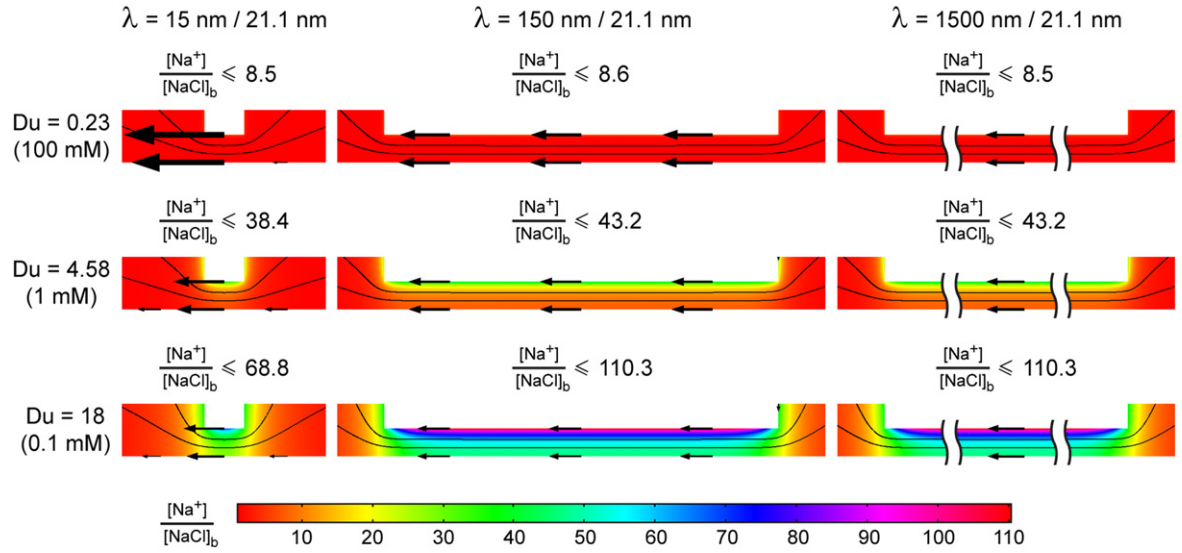

Figure 3. Electric field in a charged nanopore is impacted by short-pore effects and the uniformity of electrolyte solution inside the pore. COMSOL simulations for an axisymmetric nanopore, showing a close-up, half model with its wall and centreline, indicate that converging and diverging vectors of electric field at pore entrance and exit affect the field lines in the central region of an orifice-like nanopore ($\lambda < 1$) more than the long counterparts ($\lambda \geqslant 1$). Representing their axial component, a shorter arrow indicates a weaker field at the centreline than near the wall of the orifice-like nanopore while uniform for the long ones. In the simulations, the orifice-like and both long nanopores have the same pore radius of 10.55 nm—the mean pore radius of the 15 nm thick pnc-Si membrane used in the experiment—with the pore lengths of 15 nm, 150 nm, and 1500 nm, respectively. The color gradient signifies the concentration profile of counterions relative to bulk concentration, demonstrating the impact of the profiles near the entrance and exit of nanopore on the nanopore conductivity. Such impact can be characterized by Dukhin number, *Du*: the ratio of the electric double layer (EDL) thickness to the pore radius. (First row) for the high bulk concentration of 100 mM and low Dukhin number of $Du = 0.23$, the nanopore conductivity is governed by the conductivity of bulk solution; (second row) for the moderate concentration of 1 mM and $Du = 4.58$, with EDL starting to envelope the membrane, the mid-pore region becomes more conductive than the bulk, but the regions near the entrance and exit still have the influence of bulk solution on their conductivity; (third row) for the low concentration of 0.1 mM and high Dukhin number of $Du = 18$, with EDL strongly enveloping the entire membrane, the regions near the entrance and exit are screened from the bulk and their conductivity is governed by the conductivity of the mid-pore region.

the molar conductivity and $\bar{c}_{\pm} = \int_0^{r_i} c_{\pm} r \mathrm{d}r \Big/ \int_0^{r_i} r \mathrm{d}r$ represents the average concentration over the pore cross-sectional area.

To advance this model to short pores, the influence of the electric field at either end of the nanopore on the field in the mid-pore region is taken into account, as observed in figure 3. Considering the impact of entrance effects on the Ohmic potential first, we consider the equivalent RC parallel circuit of the porous membrane. The pore resistance $R_{\mathrm{p},i}$ in series with access resistance $R_{\mathrm{a},i}$ at either end constitutes the total resistance of each nanopore. The potential drop across the capacitor-like membrane $\Delta\phi_{\mathrm{m}}$ is equal to the sum of Ohmic potential drop across the pore $\Delta\phi_i = R_{\mathrm{p},i}\, I_i$ and those contributed by both access resistances, $2\, R_{\mathrm{a},i}\, I_i$, where I_i is the current flowing in the ith nanopore. For a charged nanopore of radius r_i, the access resistance is related to the bulk conductivity σ_{b} and surface conductivity $\sigma_{\mathrm{s},i}$ of the pore wall via Dukhin number, $Du_i = (\sigma_{\mathrm{s}}/\sigma_{\mathrm{b}})/r_i$, [19] as $R_{\mathrm{a},i} = [2 r_i \sigma_{\mathrm{b}}(2 + Du_i)]^{-1}$ [13]. Accordingly, the potential difference across each nanopore can be estimated as

$$\Delta\phi_i = \Delta\phi_{\mathrm{m}} - \frac{1}{r_i \sigma_{\mathrm{b}}\left(2 + Du_i\right)} I_i \,. \tag{2}$$

HEE originate from the converging and diverging streamlines of fluid passing through the sudden contraction and expansion at the entrance and exit of the pore. Like the extra potential drop associated with Ohmic resistances, these fluidic transitions result in additional extra pressure loss across the membrane. Assuming low Reynolds number flow, the pressure loss $\delta P_{\mathrm{p},i}$ can be approximated as the pressure drop across an orifice of zero thickness [8, 9], which is given in terms of the fluid viscosity η, pore radius r_i, and volumetric flow rate Q_i as $2\delta P_{\mathrm{p},i} = \left(3\eta/r_i^3\right) Q_i$ [25]. The total pressure differential ΔP_{m} across the membrane is given by the successive pressure drops at the entrance $\delta P_{\mathrm{p},i}$, across the pore ΔP_i, and at the exit $\delta P_{\mathrm{p},i}$ so that

$$\Delta P_i = \Delta P_{\mathrm{m}} - \frac{3\eta}{r_i^3} Q_i \,. \tag{3}$$

Incorporating the SPE described in (2) and (3) into the CLP transport equation (1) gives a set of generalized equations (SPE) describing fluid and ion transport in pores with low aspect ratio λ, while using (3) alone gives HEE transport equations. Expressed in the matrix form similar to (1), the SPE transport equations are

$$\begin{bmatrix} Q_i \\ N_i \\ I_i \end{bmatrix} = \frac{1}{l_{\mathrm{p}}} \begin{bmatrix} M_{11} & M_{12} & M_{13} \\ M_{21} & M_{22} & M_{23} \\ M_{31} & M_{32} & M_{33} \end{bmatrix} \begin{bmatrix} \Delta P_{\mathrm{m}} \\ \Delta\pi_{\mathrm{m}} \\ \Delta\phi_{\mathrm{m}} \end{bmatrix} \tag{4}$$

with the omission of the end effects on the osmotic pressure, $\Delta\pi_i \approx \Delta\pi_{\mathrm{m}}$, for the weakly charged surface of silicon (see

appendix (C) for the definition of M coefficients). Likewise, the coefficient M_{33} characterizes the conductivity of a short, charged nanopore. As an illustration of the utility of (4), consider the generalized transport equation for the ionic current I_i in the absence of the applied hydrostatic and osmotic pressure differentials. In this case only the electric field across the membrane governs the flow of ionic current in each nanopore and (4) reduces to

$$I_i = M_{33}\frac{\Delta\phi_{\mathrm{m}}}{l_{\mathrm{p}}}\,. \tag{5}$$

Given the pore tortuosity of one without loss of generality, the influence of this predicted current on the electric field $E_i = \Delta\phi_i/l_{\mathrm{p}}$ inside each nanopore indicates a possible reduction from the electric field $E_{\mathrm{m}} = \Delta\phi_{\mathrm{m}}/l_{\mathrm{p}}$ across the membrane according to (2) as

$$\frac{E_i}{E_{\mathrm{m}}} = 1 - \frac{M_{33}}{l_{\mathrm{p}} r_i \sigma_{\mathrm{b}}\left(2 + Du_i\right)}\,. \tag{6}$$

Figure 4 examines the dependence of the normalized electric field E_i/E_{m} on the pore length-to-diameter aspect ratio λ and Dukhin number Du as predicted by the SPE model. The results illustrate how the effective electric field is reduced as λ decreases or the EDL thickness increases (figure 4(a)). In either case, end effects have a greater influence on the central regions of the pore. The actual physical dimensions of a pore are not a significant determinant of the field strength. As shown in figure 4(b), the pore aspect ratio and Dukhin number nearly collapse the behavior of several curves with $\lambda = 1$ despite physical dimensions that range from nm to μm. A slight difference in the electric field for different physical dimensions arises from the increasing conductivity of electrolyte caused by the electroosmosis-induced convection $K_{33,\mathrm{conv}}$; the larger pore tends to have higher convection because of a greater hydrodynamic permeability. Note that a deviation as high as 70% from the conventional estimate E_{m} is possible for the 1-to-1 aspect ratio at high Dukhin number.

The reduced electric field (6) leads to simpler expressions under a number of limiting conditions. Approximating the total conductivity of a charged nanopore as a sum of the contributions from the bulk and its charged surface [19] leads to

$$\Lambda_+\bar{c}_+ + \Lambda_-\bar{c}_- \approx \sigma_{\mathrm{b}}\left(1 + 2Du_i\right). \tag{7}$$

Using this approximation in (6) results in a compact form of the normalized electric field as

$$\frac{E_i}{E_{\mathrm{m}}} = \left[1 + \frac{1 + 2Du_i + \left(K_{33,\mathrm{conv}}/\pi r_i^2\sigma_{\mathrm{b}}\right)}{2 + Du_i}\frac{\pi}{2\lambda_i}\right]^{-1} \tag{8}$$

(see appendix (D) for the derivation). Since the $K_{33,\mathrm{conv}}$ term in (B.10) always possesses a nonnegative value, the normalized electric field in (8) is then bounded by

$$\frac{E_i}{E_{\mathrm{m}}} \leqslant \left[1 + \frac{1 + 2Du_i}{2 + Du_i}\frac{\pi}{2\lambda_i}\right]^{-1}. \tag{9}$$

From the inequality in (9), the threshold values of the pore aspect ratio λ_i can be given as a function of the normalized electric field and Dukhin number as

$$\lambda_i \geqslant \frac{\pi}{2}\left(\frac{E_i/E_{\mathrm{m}}}{1 - E_i/E_{\mathrm{m}}}\right)\left(\frac{1 + 2Du_i}{2 + Du_i}\right). \tag{10}$$

For the normalized field of at least 0.99, λ_i must be at least $49.5\pi\ (1+2Du_i)/(2+Du_i)$, which is about 78 for $Du_i \ll 1$ or 311 for $Du_i \gg 1$.

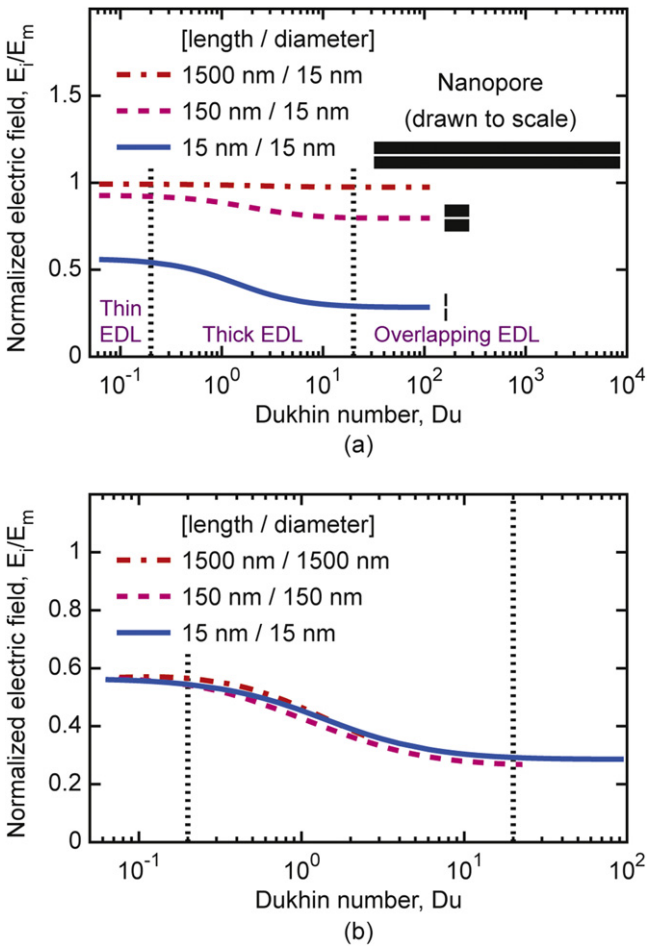

Figure 4. According to the SPE model for a single nanopore, the electric field E_i inside the nanopore normalized with its conventional estimate E_{m} across the membrane is a function of both the pore length-to-diameter aspect ratio λ and the Dukhin number Du. (a) If λ is changed, the normalized electric field is higher for the nanopore with highest value of λ; (b) in case of a fixed value of $\lambda = 1$ and multiple pore sizes, all characteristic curves are closely similar; a slight difference arises from the enhanced conductivity contributed by electroosmosis-induced convection, which more prominent for the larger pore diameter. Note that all characteristic curves saturate when the EDL is very thin or strongly overlapped.

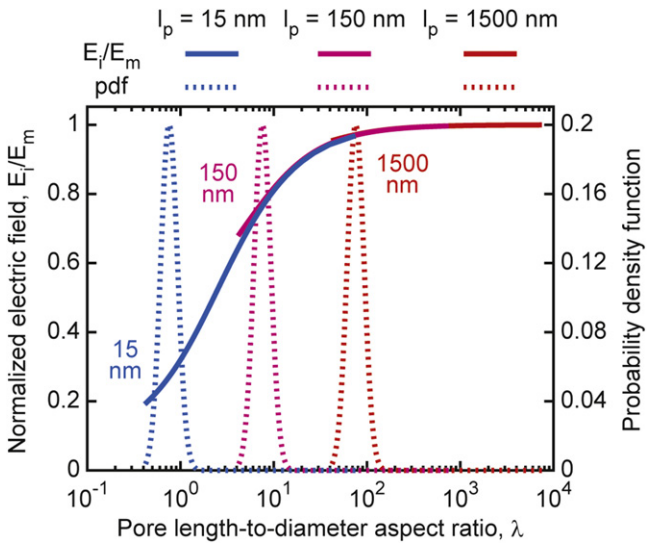

Figure 5. Localized electric fields exhibit a distribution corresponding to the pore size statistic of nanoporous membranes. For illustration purposes, assume a log-normal pore-size distribution for the 15 nm, 150 nm, and 1500 nm thick membranes. A majority of nanopores of thinner membrane have very low normalized electric fields; however, increased as the mean pore aspect ratio increases. The pore-size distribution is very important for models of ultrathin membranes, but less of a concern for those of thick membranes—as the probability density function (pdf) shifts to the right.

3.4. Electric field strength and EO flow rate for ultrathin membranes with distribution of pore sizes

For an ultrathin membrane with a distribution of pore sizes, the local electric field depends distinctively on the aspect ratio of each nanopore. Figure 5 examines the impact of a pore distribution on electric field over the membrane cross-section. Assuming a log-normal probability density function (pdf) for 15 nm, 150 nm, and 1500 nm thick membranes, the figure shows electric field reduction as a function of pore length-to-diameter aspect ratios. As the membrane becomes thicker, the effective electric field becomes more uniform, and the pore-size distribution is less of a concern.

The distribution of effective electric field in ultrathin membranes has a direct impact on the overall electroosmosis induced. This impact can be predicted by the ensemble SPE transport model that takes the pore-size distribution into account. To derive this result we modify the standard probability density function $f_R(r)$ with a probability density function $f_R^*(r)$ that describes the realistic distribution of pore sizes with a finite range and maximum pore radius r_{max}. This modification involves truncation and rescaling such that $f_R^*(r) = f_R(r) \Big/ \int_0^{r_{max}} f_R(r)\mathrm{d}r$ satisfies the normalization condition $\int_0^{r_{max}} f_R^*(r)\mathrm{d}r = 1$, while maintaining the same mean $\bar{r} = \int_0^{r_{max}} f_R^*(r) r \mathrm{d}r$ and standard deviation $r_{std} = \sqrt{\int_0^{r_{max}} f_R^*(r)(r-\bar{r})^2 \mathrm{d}r}$ of the original distribution. Incorporating this pore-size distribution into the pore-specific transport equation (4) results in the ensemble transport equations,

$$\begin{bmatrix} Q_\Sigma \\ N_\Sigma \\ I_\Sigma \end{bmatrix} = \frac{1}{l_p} \begin{bmatrix} M_{\Sigma 11} & M_{\Sigma 12} & M_{\Sigma 13} \\ M_{\Sigma 21} & M_{\Sigma 22} & M_{\Sigma 23} \\ M_{\Sigma 31} & M_{\Sigma 32} & M_{\Sigma 33} \end{bmatrix} \begin{bmatrix} \Delta P_m \\ \Delta \pi_m \\ \Delta \phi_m \end{bmatrix} \tag{11}$$

for the total flow rate Q_Σ, total solute flux N_Σ, and total current I_Σ where $M_{\Sigma jk}\left(l_p\right) = n_0 \int_0^{r_{max}} f_R^*(r) M_{jk}\left(r, l_p\right)\mathrm{d}r$ for $j, k = 1, 2, 3$ with the total number of pores n_0 derived in terms of the porosity φ and area A_m of the membrane as

$$n_0 = \frac{\varphi A_m}{\int_0^{r_{max}} f_R^*(r)\pi r^2 \mathrm{d}r}. \tag{12}$$

In the absence of the externally applied pressure and concentration differences across the membrane, the electric field E_m can be deduced from the flow rate $Q_{\Sigma,EO}$ of the purely EO transport via the coefficient $M_{\Sigma 13}$ from (11) as

$$Q_{\Sigma,EO} = n_0 \int_0^{r_{max}} f_R^*(r) K_{13}(r) \frac{E_m}{Y\left(r, l_p\right)} \mathrm{d}r\ , \tag{13}$$

where $Y = 1 + (3\eta/l_p r^3)\ K_{11} + [K_{33} + (3\eta/l_p r^3)(K_{11}K_{33} - K_{13}K_{31})]/l_p r \sigma_b (2 + Du)$ for the ensemble SPE model. In case of the derivations based on the CLP and HEE transport models, the denominator in the integral of (13) has $Y = 1$ and $Y = 1 + (3\eta/l_p r^3)\ K_{11}$, respectively. The denominator Y indicates the reduction in EO flow rate due to end effects. Note that the theoretical pore-size distribution governing all these predictions was based on the log-normal probability density function [26], which was truncated to represent the finite, maximum pore size as described previously. The EO flow rates predicted by (13) for the CLP, HEE, and SPE models are compared with the experimentally measured EO flow rates and were shown in figure 2.

4. Conclusions

The SPE model is more accurate than CLP and HEE models in predicting EO induced flow rates in ultrathin membranes. The model improvement arises from the proper estimation of the electric fields inside the membrane's orifice-like nanopores. Use of the standard electric field calculation $E_m = \Delta\phi_m/l_p$ commonly associated with EO data and CLP theory underestimates the total membrane resistance. The underestimate originates from the fact that CLP theory neglects the pore access resistance, which in the case of ultrathin membranes becomes comparable to the resistance of electrolyte inside the nanopore itself. Both types of resistance coexist, contribute to the total resistance across membrane, and result in the Ohmic potential $\Delta\phi_m$. The agreement between the SPE-based prediction and experimental measurement substantiates the novel scaling laws that the electric field is scaled not only with Dukhin number as described by the electrokinetic theory, but also with the pore length-to-diameter aspect ratio. This finding will

contribute significantly to the proper design of lab-on-a-chip systems that aim to capitalize on the low-voltage electro-osmosis from the ultrathin membranes.

Acknowledgments

This work was supported by the National Science Foundation Partnership for Innovation Program (Grant No. 11P-1237699) and National Science Foundation (PFI-BIC 1237699).

Appendix A. Experiment protocol

We measured electroosmosis through pnc-Si membranes (SiMPore, West Henrietta, NY, USA) that had a thickness of 15 nm and total area of 0.8 mm^2 with the porosity of 8.1%, mean pore radius of 10.55 nm, maximum pore radius of 18.1 nm, and standard deviation of 4.3 nm. The aqueous electrolyte solution was 1 mM NaCl and degased prior to use. The test device was custom-made to hold a 7 mm circular silicon membrane chip and allow the insertion of both electrodes into its chambers [6]. Both electrodes were made of pure silver wire coiled and coated with AGCL-675C Ag/AgCl ink (Conductive Compounds, Hudson, NH, USA). The ink was dried in the oven at 80 °C for an hour to remove all the solvents. A foot-long Teflon 1548 tubing (Upchurch Scientific, Oak Harbor, WA, USA) with an inner diameter of 500 μm was attached to the each port of the test device. All the parts were assembled under the electrolyte solution after degasing. The spacing between each electrode and the membrane was about 2 mm. Each tube was half filled with electrolyte. The assembled test device was padded dry and left stationary for 12 hours to allow the membrane to soak in the electrolyte solution. Before the measurement, the membrane pores were rinsed by pressure-driven flow with the flow rate about 1–2 $\mu L\,min^{-1}$ at 0.3–0.5 psi of the applied pressure for at least two hours. Comparing between the results from the repeated measurements with and without pore rinsing, it was found that after pore rinsing, the measured flow rates were consistent and repeatable for a given membrane. The flow velocity of liquid was measured by tracing the motion of both menisci, which were recorded under a microscope equipped with a CCD camera (Motic, British Columbia, Canada). The velocity was then multiplied by the cross-sectional area of the tube to obtain the volumetric flow rate. The DC voltage, ranging from 0.25 V to 1.5 V, was applied to the electrodes via an Agilent 33220A arbitrary waveform generator (Agilent, Santa Clara, CA, USA). This waveform generator served as an adjustable constant voltage source. The electric current flow across the membrane was monitored and recorded by an Agilent 34410A digital multimeter (Agilent, Santa Clara, CA, USA).

Appendix B. *K* coefficients for the conventional transport equations

K coefficients for the CLP transport equation (1) characterize three important lump parameters that describe the electrokinetic transports of liquid and ions in a single, infinitely long pore of radius r_i [7]. The coefficients K_{11}, K_{12}, and K_{13} characterize the flow rate Q_i of liquid solvent transport driven by the gradients of hydrostatic pressure, osmotic pressure, and applied potential, respectively. Derived by integrating the flow velocity profile over the pore cross-sectional area, these three coefficients are given as

$$K_{11}(r_i) = \frac{\pi r_i^4}{8\eta}, \tag{B.1}$$

$$K_{12}(r_i) = \frac{2\pi}{\eta} \times \int_0^{r_i}\int_r^{r_i}\int_0^{\alpha} \cosh\left[\frac{zF}{RT}\psi(\beta)\right]\frac{\beta}{\alpha} r\,d\beta\,d\alpha\,dr - \frac{\pi r_i^4}{8\eta}, \tag{B.2}$$

$$K_{13}(r_i) = \frac{2\pi zF}{\eta} \times \int_0^{r_i}\int_r^{r_i}\int_0^{\alpha} \left[c_+(\beta) - c_-(\beta)\right]\frac{\beta}{\alpha} r\,d\beta\,d\alpha\,dr. \tag{B.3}$$

The second set of K coefficients includes K_{21}, K_{22}, and K_{23}. These three coefficients characterize the ionic flux N_i contributed by every cation and anion that involve in the ionic transport inside the pore. Obtained by integrating the sum of their flux densities over the pore cross-sectional area, these three coefficients are

$$K_{21}(r_i) = \frac{\pi}{2\eta}\int_0^{r_i}\left[c_+(r) + c_-(r)\right]\left(r_i^2 - r^2\right) r\,dr, \tag{B.4}$$

$$\begin{aligned} K_{22}(r_i) = {} & \frac{2\pi}{\eta}\int_0^{r_i}\int_r^{r_i}\int_0^{\alpha}\left[c_+(r) + c_-(r)\right] \\ & \times \cosh\left[\frac{zF}{RT}\psi(\beta)\right]\frac{\beta}{\alpha} r\,d\beta\,d\alpha\,dr \\ & + \frac{\pi}{RT}\int_0^{r_i}\left\{D_+ \exp\left[-\frac{zF}{RT}\psi(r)\right]\right. \\ & \left. + D_- \exp\left[\frac{zF}{RT}\psi(r)\right]\right\} r\,dr \\ & - \frac{\pi}{2\eta}\int_0^{r_i}\left[c_+(r) + c_-(r)\right] \\ & \times \left(r_i^2 - r^2\right) r\,dr, \end{aligned} \tag{B.5}$$

$$\begin{aligned} K_{23}(r_i) = {} & \frac{2\pi zF}{\eta}\int_0^{r_i}\int_r^{r_i}\int_0^{\alpha}\left[c_+(r) + c_-(r)\right] \\ & \times \left[c_+(\beta) - c_-(\beta)\right]\frac{\beta}{\alpha} r\,d\beta\,d\alpha\,dr \\ & + \frac{2\pi zF}{RT}\int_0^{r_i}\left[D_+c_+(r) - D_-c_-(r)\right] r\,dr. \end{aligned} \tag{B.6}$$

The last three coefficients K_{31}, K_{32}, and K_{33} characterize the ionic current I_i flowing through the pore and signify the contributions from the hydrostatic pressure gradient, osmotic

pressure gradient, and electric field, respectively. Derived by integrating the net current density over the pore cross-sectional area, they are given as

$$K_{31}(r_i) = \frac{\pi z F}{2\eta}\int_0^{r_i}\left[c_+(r) - c_-(r)\right]\left(r_i^2 - r^2\right)r\mathrm{d}r, \quad \text{(B.7)}$$

$$\begin{aligned}K_{32}(r_i) =& \frac{2\pi z F}{\eta}\int_0^{r_i}\int_r^{r_i}\int_0^{\alpha}\left[c_+(r) - c_-(r)\right] \\ &\times \cosh\left[\frac{zF}{RT}\psi(\beta)\right]\frac{\beta}{\alpha}r\mathrm{d}\beta\mathrm{d}\alpha\mathrm{d}r \\ &+ \frac{\pi z F}{RT}\int_0^{r_i}\left\{D_+\exp\left[-\frac{zF}{RT}\psi(r)\right]\right. \\ &\left. - D_-\exp\left[\frac{zF}{RT}\psi(r)\right]\right\}r\mathrm{d}r \\ &- \frac{\pi z F}{2\eta}\int_0^{r_i}\left[c_+(r) - c_-(r)\right] \\ &\times\left(r_i^2 - r^2\right)r\mathrm{d}r, \end{aligned} \quad \text{(B.8)}$$

$$K_{33}(r_i) = K_{33,\mathrm{conv}}(r_i) + K_{33,\mathrm{em}}(r_i), \quad \text{(B.9)}$$

$$\begin{aligned}K_{33,\mathrm{conv}}(r_i) =& \frac{2\pi z^2F^2}{\eta}\int_0^{r_i}\int_r^{r_i}\int_0^{\alpha}\left[c_+(r) - c_-(r)\right] \\ &\times\left[c_+(\beta) - c_-(\beta)\right]\frac{\beta}{\alpha}r\mathrm{d}\beta\mathrm{d}\alpha\mathrm{d}r, \end{aligned} \quad \text{(B.10)}$$

$$K_{33,\mathrm{em}}(r_i) = \frac{2\pi z^2F^2}{RT}\int_0^{r_i}\left[D_+c_+(r) + D_-c_-(r)\right]r\mathrm{d}r. \quad \text{(B.11)}$$

Note that K_{33} represents the conductivity of electrolyte solution inside a charged pore where $K_{33,\mathrm{conv}}$ and $K_{33,\mathrm{em}}$ denote the contributions from the convection and electromigration, respectively.

Appendix C. *M* coefficients for the generalized transport equations

M coefficients for the generalized transport equations based on the model of SPE (4) describes the electrokinetic transports of liquid and ions in a single pore of radius r_i and finite length l_p. Deriving from the CLP transport equation (1), taking SPE given by (2) and (3) into account transforms the pore-specific to membrane-oriented parameters as

$$\begin{aligned}\begin{bmatrix}\Delta P_i \\ \Delta\pi_i \\ \Delta\phi_i\end{bmatrix} =& \begin{bmatrix}\Delta P_\mathrm{m} \\ \Delta\pi_\mathrm{m} \\ \Delta\phi_\mathrm{m}\end{bmatrix} - \begin{bmatrix}3\eta r_i^{-3} & 0 & 0 \\ 0 & 0 & 0 \\ 0 & 0 & \left[r_i\sigma_\mathrm{b}\left(2 + Du_i\right)\right]^{-1}\end{bmatrix} \\ &\times\begin{bmatrix}Q_i \\ N_i \\ I_i\end{bmatrix}. \end{aligned} \quad \text{(C.1)}$$

Note the omission of the end effects on the osmotic pressure, $\Delta\pi_i \approx \Delta\pi_\mathrm{m}$, for the weakly charged surface of silicon. Substituting this transformation back into (1) and rearranging terms yield the generalized transport equation (4) with the *M* coefficients taking the form of

$$\begin{aligned}&\mathbf{M} \\ &= \frac{1}{l_\mathrm{p}}\left(\mathbf{I} + \frac{1}{l_\mathrm{p}}\mathbf{K}\begin{bmatrix}3\eta r_i^{-3} & 0 & 0 \\ 0 & 0 & 0 \\ 0 & 0 & \left[r_i\sigma_\mathrm{b}\left(2 + Du_i\right)\right]^{-1}\end{bmatrix}\right)^{-1}\mathbf{K}, \end{aligned} \quad \text{(C.2)}$$

where **I**, **M**, and **K** represent an identity matrix, the matrix of *M* coefficients in (4), and the matrix of *K* coefficients in (1) and listed in appendix B, respectively.

Appendix D. Derivation of the approximated normalized electric field

Substituting coefficient M_{33} in (6), the normalized electric field is given in terms of *K* coefficients defined in appendix (B) as

$$\frac{E_i}{E_\mathrm{m}} = \left[1 + \frac{K_{33} - \dfrac{24\eta}{\left(8l_\mathrm{p}r_i^{-1} + 3\pi\right)r_i^4}K_{13}K_{31}}{l_\mathrm{p}r_i\sigma_\mathrm{b}\left(2 + Du_i\right)}\right]^{-1}. \quad \text{(D.1)}$$

Since the conductivity contributed by the concentration profiles inside a nanopore is usually much larger than that contributed by the hydrodynamic convection, the normalized field can be approximated as

$$\frac{E_i}{E_\mathrm{m}} \approx \left[1 + \frac{K_{33}}{l_\mathrm{p}r_i\sigma_\mathrm{b}\left(2 + Du_i\right)}\right]^{-1}. \quad \text{(D.2)}$$

From (B.9) and (B.11), the coefficient K_{33} can be given as $K_{33} = \pi r_i^2\left(\Lambda_+\bar{c}_+ + \Lambda_-\bar{c}_-\right) + K_{33,\mathrm{conv}}$, where the average concentrations of cation and anion is defined as $\bar{c}_\pm = \int_0^{r_i} c_\pm r\mathrm{d}r \Big/ \int_0^{r_i} r\mathrm{d}r$ with their molar conductivities, $\Lambda_\pm = F^2D_\pm/RT$. Using the approximated conductivity of a charged nanopore (7) the normalized electric field has a compact form as

$$\frac{E_i}{E_\mathrm{m}} \approx \left[1 + \frac{1 + 2Du_i + K_{33,\mathrm{conv}}\big/\pi r_i^2\sigma_\mathrm{b}}{2 + Du_i}\frac{\pi}{2\lambda_i}\right]^{-1}, \quad \text{(D.3)}$$

where $\lambda_i = l_\mathrm{p}/2r_i$ represents the pore length-to-diameter aspect ratio.

References

[1] Lee C-Y, Lee G-B, Lin J-L, Huang F-C and Liao C-S 2005 *J. Micromech. Microeng.* **15** 1215–23

[2] Wang C, Wang L, Zhu X, Wang Y and Xue J 2012 *Lab Chip* **12** 1710–6

[3] Litster S, Suss M E and Santiago J G 2010 *Sensors Actuators A* **163** 311–4

[4] Guo Q, Liu Y, Wu X and Yang J 2009 *Microsyst. Technol.* **15** 1009–15

[5] Ai Y, Yalcin S E, Gu D, Baysal O, Baumgart H, Qian S and Beskok A 2010 *J. Colloid Interface Sci.* **350** 465–70
[6] Snyder J L, Getpreecharsawas J, Fang D Z, Gaborski T R, Striemer C C, Fauchet P M, Borkholder D A and McGrath J L 2013 *Proc. Natl. Acad. Sci. USA* **110** 18425–30
[7] Gross R J and Osterle J F 1968 *J. Chem. Phys.* **49** 228–34
[8] Dagan Z, Weinbaum S and Pfeffer R 1982 *J. Fluid Mech.* **115** 505–23
[9] Zhang Y, Gu X-J, Barber R W and Emerson D R 2004 *J. Colloid Interface Sci.* **275** 670–8
[10] Chakraborty S and Padhy S 2008 *J. Phys. D: Appl. Phys.* **41** 065502
[11] Hille B 1968 *J. Gen. Physiol.* **51** 199–219
[12] Hall J E 1975 *J. Gen. Physiol.* **66** 531–2
[13] Lee C, Joly L, Siria A, Biance A-L, Fulcrand R and Bocquet L 2012 *Nano Lett.* **12** 4037–44
[14] Khair A S and Squires T M 2008 *J. Fluid Mech.* **615** 323–34
[15] Baldessari F and Santiago J G 2008 *J. Colloid Interface Sci.* **325** 526–38
[16] Striemer C C, Gaborski T R, McGrath J L and Fauchet P M 2007 *Nature* **445** 749–53
[17] Fievet P, Szymczyk A, Aoubiza B and Pagetti J 2000 *J. Membr. Sci.* **168** 87–100
[18] Yao S, Hertzog D E, Zeng S, Mikkelsen J C Jr and Santiago J G 2003 *J. Colloid Interface Sci.* **268** 143–53
[19] Delgado A V, González-Caballero F, Hunter R J, Koopal L K and Lyklema J 2007 *J. Colloid Interface Sci.* **309** 194–224
[20] Yates D E, Levine S and Healy T W 1974 *J. Chem. Soc. Faraday Trans.* **1** 1807–18
[21] Ninham B W and Parsegian V A 1971 *J. Theor. Biol.* **31** 405–28
[22] Behrens S H and Grier D G 2001 *J. Chem. Phys.* **115** 6716–21
[23] Grahame D C 1947 *Chem. Rev.* **41** 441–501
[24] Westall J and Hohl H 1980 *Adv. Colloid Interface Sci.* **12** 265–94
[25] Sampson R A 1891 *Phil. Trans. R. Soc.* A **182** 449–518
[26] Zydney A L, Aimar P, Meireles M, Pimbley J M and Belfort G 1994 *J. Membr. Sci.* **91** 293–8